

Two- and Three-Dimensional Finite Element Analyses of Crack Fronts in a Multidirectional Composite ENF Specimen

R. Krüger, S. Rinderknecht and M. König

ISD-Report No. 97/1, May 1997

Abstract

Results are presented from a numerical investigation of the effect of the shape of the delamination front on energy release rate distribution in a laminated carbon fibre reinforced epoxy end-notched flexure test specimen. The deformation behaviour of the specimen has been computed by three-dimensional nonlinear finite element analyses using a recently developed layered 3D-shell element. The distributions of the local mixed mode energy release rates along the initial straight and one measured curved delamination fronts have been determined by the virtual crack closure method. The dependency of computed total energy release rate as well as the individual mode contributions from the shape of the delamination front is discussed. By means of 2D models for which a delamination process element has been used, a curved front was iteratively determined along which the total energy release rate is constant. The shape of this front is in good agreement with experimentally observed front shapes.

Keywords: Composite materials, delamination, energy release rate, nonlinear finite element analysis, 3D layered shell element, delamination process element, virtual crack closure method, moving mesh technique

Nomenclature

Symbol	Meaning
a :	crack length
A :	created crack surface
A :	extended membrane stiffness
A_{ij} :	stiffness coefficient of A matrix
B :	total width of specimen
B :	coupling stiffness
B_{ij} :	stiffness coefficient of B matrix
C :	material stiffness
C_{ij} :	stiffness coefficient of C matrix
D :	flexural stiffness
d :	delamination
D_{ij} :	stiffness coefficient of D matrix
E_i :	Young's modulus
G_i :	energy release rate for mode i
G_{ij} :	shear modulus
h :	half of the total specimen thickness
L :	half of the total specimen length
M_{ij} :	moment resultant
N_{ij} :	force resultant
P :	external loading
P_c :	critical load at crack propagation
Q' :	off-axis three-dimensional stiffness
s :	local coordinate along front
t :	ply thickness
t_p :	thickness of process layer
u :	displacement
u_i :	nodal point displacement at node i , x-direction
v_i :	nodal point displacement at node i , y-direction
w :	normalized width

Symbol	Meaning
w_i :	nodal point displacement at node i , z-direction
X_i :	nodal point force at node i , x-direction
y :	width coordinate of specimen
Y_i :	nodal point force at node i , y-direction
z :	distance from element mid-plane
Z_i :	nodal point force at node i , z-direction
Δa_i :	length of element i at the crack tip
ΔA_i :	crack surface area virtually closed
$\Delta u_i, \Delta v_i, \Delta w_i$:	relative displacements at node i ,
ϵ_{ij} :	strain
θ :	angle of ply orientation
κ_{ij} :	curvature
ν_{ij} :	Poisson's ratio
σ_{ij} :	stress
ψ :	damage parameter

1 Introduction

Motivated by the increasing use of composites in primary structural components, research has been focussed on the disbond of two adjacent fibre reinforced layers of a laminate, which is a prevalent state of damage, commonly known as *delamination*. A recent survey on problems concerning composite parts of civil aircraft shows that delamination, mainly caused by impact, presents 60% of all damage observed [1]. In a 1991 IATA survey, air carriers reported that about 40% of all damages come from platform or ground handling and maintenance [2]. Up to now, failure caused by delamination is prevented by using empirically determined design criteria – based on maximum allowable strains (usually 0.3%) – during layout and construction of components made of fibre reinforced materials [3, 4, 5]. For an optimal utilisation of the potential offered by those materials as well as for the determination of inspection intervals, however, it is essential to be able to predict delamination propagation.

In this investigation, criteria based on fracture mechanics are used to describe the delamination failure. Propagation therefore is to be expected when a function of the mixed mode energy release rates G_I , G_{II} and G_{III} along the delamination front locally exceeds a certain critical value, G_c . This value can be regarded as a property of the interface and depends on the material and on the ply orientations of the layers adjacent to the plane of delamination.

For the experimental determination of critical energy release rates, G_c , several simple test specimens have been developed. These include the double cantilever beam (DCB) specimen for determination of G_{Ic} , and the end-notched flexure (ENF) specimen for G_{IIc} (figure 1). The mixed mode bending (MMB) specimen [6] and the recently introduced single leg bending (SLB) specimen [7] have both been used for the investigation of mode I and mode II interaction.

In general, DCB, ENF and mixed mode tests are performed on unidirectionally reinforced laminates, which means that delamination growth occurs at a [0/0] interface and crack propagation is parallel to the fibers. This kind of delamination growth, however, will rarely occur in real structures. Previous investigations indicate that the experimentally determined critical energy release rate at any mode mix is sensitive to the ply orientations at the interface. Thus, it is of considerable importance to evaluate G_c at interfaces with dissimilar ply orientations if approaches based on fracture mechanics will be used for future design purposes. Systematically investigating all possible relative interfacial orientations would be impractical. However, evaluating the critical energy release rate using a number of selected interfaces could provide a measure of the *minimum* value. This value would be appropriate for use in design.

A number of experimental studies have been performed [8, 9, 10] where the critical energy release rates of various interfaces have been evaluated under mode I, mode II and mixed-mode conditions. However, three-dimensional effects can result in nonuniform energy release rate and mode ratio distributions across the width of a delamination toughness test specimen [11, 12, 13]. This can cause the true toughness to be quite different from values obtained by two-dimensional analyses and corresponding data reduction techniques. These three-dimensional effects have been quantified in a previous investigation based on three-dimensional finite element analysis [14].

The goal of the investigation presented herein is to

- verify that predicting the development of size and shape of a growing delamination is possible by using a fracture mechanics based approach
- supply input data to set up a predictive model for onset and growth of a delamination located between layers of dissimilar orientations
- verify that the shape of the delamination front of an ENF specimen is controlled by $G(s) = G_{II} + G_{III} = \text{const.}$
- use the delamination process element in combination with a moving mesh technique to iteratively compute a delamination contour along which $G(s) = \text{const.}$

2 Methodology and Analysis Tools

The most significant step for the current approach is the computation of the distribution of the mixed mode energy release rates along arbitrarily shaped delamination fronts, which means that a classical analytical evaluation of energy release rates – as possible for geometrically simple cases – is not applicable. Computational methods based on finite element (FE) modelling are a meaningful and efficient tool by which the energy release rate at delamination growth along the entire delamination front can be evaluated.

2.1 A Continuum-Based 3D-Shell Element

Due to the extensive computation times already noticeable for 3D-models of simple DCB- and ENF-specimens [13], the development of a *layered volume element* using a continuum-based three-dimensional shell theory [15] has been found to be necessary as

- the computation of the complete load path using a layer of brick elements for each ply of the specimen will be extremely computer time consuming
- the standard isoparametric eight- as well as twenty-noded volume elements have the tendency to lock for small element thickness to element length ratios, leading to an unnaturally stiff behaviour of the structure during computation
- a volume-type element with eight nodes is necessary to assure complete compatibility with the contactor and target elements that are used to avoid structural overlapping in the vicinity of the crack front.

Several orthotropic layers of different orientations may be included in the developed layered 3D-shell element. An extended three-dimensional *ABD*-Matrix has to be supplied by the user as an

input. The individual components of the matrix are calculated as for classical laminated plate theory [16] with

$$\begin{aligned} \mathbf{A} &= \sum_{i=1}^m \mathbf{Q}^{(i)} \cdot [z^{(i)} - z^{(i-1)}] \\ \mathbf{B} &= \frac{1}{2} \cdot \sum_{i=1}^m \mathbf{Q}^{(i)} \cdot [(z^{(i)})^2 - (z^{(i-1)})^2] \\ \mathbf{D} &= \frac{1}{3} \cdot \sum_{i=1}^m \mathbf{Q}^{(i)} \cdot [(z^{(i)})^3 - (z^{(i-1)})^3] \end{aligned}$$

where \mathbf{A} denotes the extended membrane stiffness, \mathbf{D} the flexural stiffness, \mathbf{B} the coupling stiffness, $\mathbf{Q}^{(i)}$ the off-axis three-dimensional stiffness of the i -th ply and $z^{(i)}$ and $z^{(i-1)}$ the distances of the surfaces of the i -th ply from the element mid-plane as shown in figure 2. We thus obtain the three-dimensional relationship

$$\begin{bmatrix} N_{ij} \\ M_{ij} \end{bmatrix} = \begin{bmatrix} A_{ij} & B_{ij} \\ B_{ij} & D_{ij} \end{bmatrix} \cdot \begin{bmatrix} \varepsilon_{ij} \\ \kappa_{ij} \end{bmatrix} \quad i, j = 1, 6$$

where the N_{ij} and M_{ij} denote the force and moment resultants, the A_{ij} , B_{ij} and D_{ij} the stiffness coefficients and the ε_{ij} and κ_{ij} the strains and curvatures, respectively.

The first numerical tests of this element were performed using models of unidirectionally laminated DCB and ENF specimens. These were chosen for study as they had previously been investigated using FE-models consisting of brick elements with 20 nodes [13]. These analyses were repeated using the layered 3D-shell element. This yielded the same results for the energy release rates but simultaneously reduced the computation time up to a factor of six. Additionally, energy release rates were computed for DCB and ENF specimens with quasi-isotropic layup to test the possibility of grouping several layers of different orientations in one element [14].

2.2 Virtual Crack Closure Method

It has been found that the virtual crack closure method is most favourable for the computation of energy release rates, because the separation of the total energy release rate into the contributions by the different crack opening modes is possible in a straight forward manner [17, 18]. When using this method, only one FE-computation is necessary for a given delamination front, which is beneficial especially when solving large, geometrically non-linear problems.

When using eight-noded elements – such as the 3D-shell element described in the next section – the procedure for the computation of the energy release rates can be illustrated by figures 3 and 4. The crack is virtually closed along the entire delamination front over the distance Δa_1 . The energy release rate which is computed for the area ΔA is assigned to node 1' on the crack front. This is mainly done to obtain the value at a nodal point of the FE-mesh, which simplifies data management for postprocessing. For a specimen containing an arbitrarily shaped delamination contour, which is automatically meshed by commercially available software, however, it is not useful to assume an equal element area ΔA along the entire front. Therefore, in the most general

case where the element widths b_i as well as the element lengths Δa_i may vary, the relative displacements $\Delta u_1, \Delta v_1$ and Δw_1 computed at node 1 behind the crack front for an element length Δa_1 have to be corrected to fit to the forces $X_{1'}, Y_{1'}$ and $Z_{1'}$ computed directly at the front (node 1') for an element length Δa_2 . This may be done by taking into account the shape functions of the elements. For volume elements with eight nodes, the displacements vary linearly along the edges and we obtain the desired values which correspond to the computed forces at point 1' by linear interpolation ($\Delta a_1 > \Delta a_2$) or linear extrapolation ($\Delta a_1 < \Delta a_2$) of the computed displacements at point 1. Furthermore, allowing a variation of the element widths b_i requires an adjusted calculation of the adjacent element surfaces according to $\Delta A_i = \frac{1}{2} \cdot \Delta a_1 \cdot b_i$.

We thus obtain

$$\begin{aligned} G_I &= \frac{1}{2} \cdot \frac{1}{\Delta A_1 + \Delta A_2} Y_{1'} \cdot \Delta v_1 \cdot \frac{\Delta a_2}{\Delta a_1} \\ G_{II} &= \frac{1}{2} \cdot \frac{1}{\Delta A_1 + \Delta A_2} X_{1'} \cdot \Delta u_1 \cdot \frac{\Delta a_2}{\Delta a_1} \\ G_{III} &= \frac{1}{2} \cdot \frac{1}{\Delta A_1 + \Delta A_2} Z_{1'} \cdot \Delta w_1 \cdot \frac{\Delta a_2}{\Delta a_1}. \end{aligned}$$

Other techniques for virtually closing the crack along the crack front are mentioned in [19, 20].

Mathematical solutions of the near crack tip field indicate that stresses start to oscillate in the immediate vicinity of the tip when crack growth occurs at interfaces between materials with dissimilar properties. These solutions, however, allow the crack surfaces to interpenetrate, which is physically not correct. A non-convergence of the virtual crack closure method associated with the oscillatory singularity has been observed in previous investigations [21, 22]. Convergence studies carried out on ENF and SLB specimens where crack propagation occurs between layers of different orientations did not show the reported non-convergence [14]. This may be due to a very small bimaterial mismatch of the considered interfaces [23]. The issue will be investigated further.

2.3 A Contact Processor to Avoid Interpenetration in the 3D-Models

Local contact occurring in the delaminated area is a phenomenon that has to be considered in each model used for investigating the delamination behaviour. In the zone of contact the delaminated sublaminates is locally supported by the base laminate influencing the deformation behaviour of the sublaminates. Using classical linear elastic finite element analysis, this phenomenon can not be simulated, as an interpenetration of the different layers may not be prevented. Therefore, a non-linear analysis becomes necessary if the contact problem has to be taken into account.

The contact processor employed accounts for frictionless contact of deformable bodies by applying the penalty method [24]. One of the bodies serves as a so-called contactor, the other as the target as shown in figure 5. The contact problem is described using two independent meshes, one applied to the surface of the three-dimensional mesh representing the body of the contactor the other to the surface of the corresponding mesh of the target. This is done to keep the description of the surfaces involved fairly simple. It should be mentioned that these surface elements are not

structural elements in the common sense as they do not introduce additional degrees of freedom. Therefore, these surface elements are initialized and handled separately. Although the setup is arbitrary, it is suggested – for mere numerical reasons – to choose the softer body to serve as the contactor. The nodal points connected to the mesh of the contactor are called dependent nodes, those belonging to the mesh of the target are called guiding nodes. A dependent node can touch a target element which is defined by the guiding nodes along its edges. Using the penalty method, the amount of contact is directly controlled by the penalty factor. This allows for a user control of the process from the soft side, which is advantageous for many applications. On the other hand, this may also lead to numerical problems if the penalty factor has been chosen too large. In most cases, it is helpful to start with a small penalty factor which then has to be increased once equilibrium is reached. It has to be considered, however, that the state of equilibrium which can be attained depends on the penalty factor chosen. It is possible that the iteration stops due to the fact that the penalty factor chosen is too small, thus avoiding further iterations to reach a smaller error.

Looking at figure 5, the kinematics of the problem can easily be explained. Three dependent nodes have penetrated the target, violating the contact conditions and thereby creating active contact elements during the finite element computation. An active element consists of the dependent node and the target element involved. The computed stiffness matrix provides the relationship between the contacting bodies and the resulting contact forces. It has to be considered that the contact elements should be kinematically compatible with those elements they are attached to, thus transmitting the forces of the base elements in a kinematically compatible manner. The algorithm used has to push the nodes onto the target surface following a vector normal to this surface. The intersection with the surface yields the physical location C of the contact. The length of the vector is equal to the distance. In a numerical analysis contact with a surface can only be achieved within certain limits, the dependent node will always slightly penetrate even if equilibrium is reached. Therefore, the distance is important when checking for the contact conditions. Looking at figure 5, we notice that a dependent node is free if the distance is greater than zero and is in contact or penetrates once this distance becomes negative. Defining the maximum allowable penetration as gap , the kinematics of the contact problem can be described as follows:

- distance > 0 : the dependent node is free
- $gap < distance < 0$: the dependent node is in contact
- distance $< gap$: the dependent node has violated the contact condition and has penetrated. It therefore needs to be brought back to the target surface.

The maximal allowable penetration depth gap is a parameter, the value of which is to be set by the individual user.

The contact processor employed allows each of the dependent nodes to get into contact with each of the target elements, therefore the size and required space of the problem to be analyzed depends on the maximum difference in nodal point numbers of the surface meshes involved. In order to save space and computation time it is therefore advisable not to extend the area meshed beyond the zone of expected contact and further to carefully choose the numbering of the nodal points.

2.4 Two-Dimensional Delamination Growth Simulation

Owing to the high computational effort using three-dimensional models, a finite element model based on the Reissner-Mindlin plate theory is used in addition for simulation of delamination growth. The so-called delamination process element [25] incorporates both the sublaminates and the base laminate as well as a process layer to which the process of delamination growth is spatially restricted (figure 6). Owing to the possibility of specifying the damage state in the material law of the process layer

$$\sigma_{ij} = (1 - \psi) \cdot C_{ij} \cdot \varepsilon_{ij} \quad \text{with } 0 \leq \psi \leq 1 ,$$

the structure may be modelled with only one element over the laminate thickness. Furthermore, the element formulation allows the consideration of contact between sublaminates and base laminate, which is realized by a special control mechanism in the process layer [25].

The virtual crack closure method is again applied to this two-dimensional model in order to calculate energy release rates. However, the mode separation leads to unreliable results, because the local kinematics in the immediate vicinity of the delamination front cannot be handled accurately. Nevertheless, good results are obtained for the total energy release rate G_T which depends only on the global energy released by the entire structure and is thus not significantly affected by local errors along the front.

For the simulation of delamination growth, the Griffith growth criterion $G_T \geq G_c$ is used. In this physically nonlinear calculation, the growth criterion may only be checked along the delamination front and thus, this front has to be traced during the iterative computation in each load step. Physically, it is assumed that a point on the delamination front starts to move if $G_T > G_c$ and stops again as soon as $G_T = G_c$ is reached. The moving delamination front is realized using a moving mesh technique, in which the mesh is geometrically adapted to the delamination front after the delamination front nodes, moving on fictitious straight lines, are positioned (figure 7). The mesh topology as well as the element node values of the damage parameter do not change. Each delamination front node possesses only one motional degree of freedom and thus, the solution procedure becomes very simple [26].

A delamination front contour with $G(s) = const.$ may hence be calculated with this model when the delamination growth simulation is performed up to a state in which the entire front is growing. The iterated equilibrium conditions of each load step are then characterized by $G_T = G_c$ along the entire front.

3 Analyses of ENF Specimen with Multidirectional Layup

A number of experimental studies have been performed where the critical energy release rates of various interfaces are evaluated under mode I, mode II and mixed-mode conditions. However, three-dimensional effects can result in nonuniform energy release rate and mode ratio distributions across the width of delamination toughness test specimens [11, 12, 13], which can cause the true toughnesses to be quite different from those obtained by two-dimensional analyses and corresponding data reduction techniques. For example, in the mode II end-notches flexure (ENF) test, it has

been shown in previous investigations that for a straight delamination front, the mode II energy release rate is highest at the edges of a specimen and lowest at its centre, and that the regions of peak mode II near the edges are accompanied by mode III components [13, 14]. Both of these effects are caused primarily by anticlastic bending. All commonly used data reduction techniques for the ENF test implicitly assume self-similar, mode II delamination propagation from an initially introduced straight crack front. Therefore, minimization of the mode III contribution will lead to a minimized error of the G_{IIc} value as obtained experimentally from load versus deflection data.

For multidirectional laminates, a total of five different stacking sequences and four different interfaces at which delamination growth occurs, namely [+15/+15], [+15/-15], [+30/+30] and [+30/-30], have been investigated experimentally in [8, 9, 10, 27]. In addition, the two unidirectional layups $[0]_{30}$ and $[0]_{32}$ were included. Previous numerical investigations and final conclusions and recommendations resulting from these experimental-numerical studies are published in [14, 28, 29, 30].

3.1 Material and Geometrical Data

The current investigation is entirely focussed on an ENF specimen where crack propagation occurs between a [+30] and a [-30] layer. The following material data were assumed for the fibre matrix combination Ciba-Geigy C12K/R6376 (notation according to Tsai [16] with subscript 1 denoting the fibre direction):

$$\begin{aligned}
 E_1 &= 146860 \text{ N/mm}^2 \\
 E_2 = E_3 &= 10620 \text{ N/mm}^2 \\
 E_5 = E_6 = G_{31} = G_{12} &= 5450 \text{ N/mm}^2 \\
 \nu_{21} &= 0.33 \\
 \nu_{23} &= 0.33 \\
 t \text{ (ply thickness)} &= 0.127 \text{ mm}
 \end{aligned}$$

Layup: $[\pm 30 / (\mp 30)_2 / (\pm 30)_2 / \mp 30 / d / (\mp 30) / (\pm 30)_2 / (\mp 30)_2 / \pm 30]$
(symbol d denotes the location of the delamination)

Thickness: $2h = 3.05 \text{ mm}$

Length: $2L = 101.6 \text{ mm}$

Width: $B = 25 \text{ mm}$

Crack length: $a = 28.6 \text{ mm}$

3.2 3D-Computation of Energy Release Rates Along Initial Delamination Front

Due to the existence of $[\pm 30]$ plies, models extending across the entire width of the ENF specimen have to be used, as shown in figure 8. As shown in the cutout, eight elements were used over the thickness of the specimen, where the two plies above and the two plies below the plane of

delamination were modelled with one element over the thickness of each ply, and the outer layers were modelled by grouping several plies together into an element. Across the width of the specimen, a 1.0 mm wide section on both edges was modelled using five elements, whereas the centre part of the specimen (≈ 23 mm) was divided into twelve elements. Based on earlier investigations [14], penetration of the arms was prevented by introducing an artificial second support as shown schematically in figure 9, thus avoiding the contact analysis. The typical deformation behaviour of an ENF specimen, as computed, is shown in figure 10. Looking at the distribution of the energy release rates G_{II} and G_{III} , plotted versus the normalized width w of the specimen defined as

$$w = \frac{B-y}{B} = 1 - \frac{y}{B} \quad ,$$

we basically notice the same overall distribution (figure 11) as obtained for UD-layups [13, 14]. The peaks at the edges of the specimen, however, are more pronounced for interface angles of 30° than for UD-layups, causing the straight front to grow into a curved delamination front. The three-dimensional effects, which become visible in the distribution of the energy release rates across the width of ENF specimens, have been thoroughly investigated in related studies. Resulting design recommendations for ENF specimen are to be found in [28, 30].

3.3 Energy Release Rates Along an Experimentally Observed Front

From observations made for DCB specimens [13, 14], it is to be expected that the pronounced peaks of G_{II} and G_{III} in a fairly large zone near the edges of the ENF specimen and the resulting smaller zone with a nearly constant distribution in the centre cause the straight front to grow into a curved delamination front (inverse thumb nail shape). This prediction is verified by experiments where the fronts have been made visible by ultrasonic C-scan. As an example, a front is shown which developed at 99.9% of the critical load, immediately before unstable propagation occurred (see figure 12 from [10]). Due to the lack of a sufficient number of C-scans, it was not possible to obtain an averaged and smoothed front, and therefore, the front of figure 12 was used as input to an FE-model, a detail of which is shown in figure 13. As for the previous case, eight elements were used over the thickness of the specimen. The two plies directly above and the two plies directly below the delamination were modelled individually. The remaining layers were modelled by grouping several plies together into an element. Across the width of the specimen, a 5.0 mm wide section on both edges, where the curvature of the front is pronounced, was modelled using ten elements, whereas the centre part of the specimen (≈ 15 mm), where the front is relatively smooth, was divided into twelve elements. When applying boundary conditions as shown in figure 9, interpenetration of the cantilever arms occurred in the immediate vicinity of the crack tip. Hence, the computation had to be repeated using the contact processor described in section 2.3.

Based on previous investigations which focussed on the crack growth in DCB and ENF specimens [13, 14], it could be assumed that the originally straight front would grow into a curved front along which G_{II} is constant and G_{III} negligible. This expected curved front is in fact observed. The computed energy release rates, as plotted in figure 14, showing a significant mode III contribution, suggest, however, that the conditions along the front s may not be described by $G(s) = G_{II} = G_{III} = const$. Looking at the distribution of the total energy release rate G_T in figure 14, we notice that the computed values are scattered around an average value. Taking into account that the front

investigated is arbitrarily chosen and has a random, unsmoothed shape, a form $G(s) = G_{II} + G_{III} = G_T = \text{const.}$ is more likely to describe the propagated front.

3.4 2D-Simulation of Delamination Growth

This simulation of delamination growth is based on the criterion $G_T = G_c = \text{const.}$, with $G_c = 1.4 \text{ kJ/m}^2$, employing the delamination process element of section 2.4. Firstly, delamination growth was analyzed using a rather coarse mesh with 11 equidistant nodes along the delamination front. Figures 15 and 16 show the calculated load-deflection behaviour, the magnified structural deformation as well as the mesh movement. On the projected surfaces underneath the meshes, the grey shaded areas represent the grown delamination. In agreement with the experimental investigations, the application of the Griffith criterion leads to a curved front with increasing delamination growth from the centre towards the edges of the specimen. Furthermore, stable delamination growth is observed up to growth position 2, where a sudden change to unstable growth occurs. As the load-growth behaviour of figure 17 shows, this transition point is caused by the beginning of delamination growth at the front centre i.e. delamination growth occurring along the entire front.

A second delamination growth simulation was performed using a fine mesh with 23 nodes along the delamination front, distributed with decreasing distance towards the edges (figure 18). Thus a better discretization of a delamination front along which the total energy release rate is constant may be achieved. In this simulation, the converged delamination contour obtained with the coarse mesh for a load of 670 N (at the unstable growth path) was used as a start contour and a new contour was iterated for a load of 650 N (figure 19). Comparing the results obtained with the coarse and the fine mesh (figure 20), we see a significant spatial deviation of the front positions calculated for the same load of up to about 1 mm, but a small difference (less than 3%) in the equilibrium load for fronts with approximately the same spatial position.

Furthermore, a high sensitivity of the energy release rate distribution with respect to the contour shape is observed. Although the two contours of figure 21 (both discretized with the fine mesh) show very small spatial deviations, the distributions of the total energy release rate differ significantly (figure 22). Hence, the analysis of experimentally measured individual contours may lead to a significant deviation from a constant energy release rate distribution, although the applied growth criterion might be well-suited to describing the overall structural behaviour in a delamination growth simulation.

Employing now the delamination front as iterated for the condition of constant G_T and reducing the load to 99.9% of the peak load observed experimentally for the specimen of figure 12 (see section 3.3) results in the energy release rate distribution shown in figure 23. It is remarkable that both G_{II} and G_{III} vary significantly over the width of the specimen, whereas G_T is constant.

3.5 3D-Computation of Energy Release Rates Along the Simulated Front

The iteratively computed curved front along which the total energy release rate is constant (front calculated with fine mesh in section 3.4) was used as input for a three-dimensional analysis. A

detail of the finite element mesh used is shown in figure 24. The typical deformation behaviour of the ENF specimen, as computed, is shown in figure 25. Looking at the distribution of the energy release rates plotted in figure 26, it is found that a fairly constant G_T -distribution is observed along the front. The deviations from a perfectly constant line are caused by the input for the crack front coordinates. A total of 23 values, as obtained from the investigation in section 3.4, was used as input; the contour itself was obtained as a fit. These minor deviations from the contour iterated in section 3.4 may significantly influence the computed energy release rates along the front (compare section 3.4). The discrepancy in the zones close to the free edges may in addition be caused by the basic difference between the two models. The delamination process element model is not able to capture the local stresses in the thickness direction which occur near the free edges. The 3D-shell element, however, accounts for these stresses. This may lead to the fluctuations in computed energy release rate in this area.

4 Conclusions and Outlook

In the present paper, results have been presented from a numerical investigation of the effect of delamination front shape on energy release rate distribution in a laminated carbon fibre reinforced epoxy end-notched flexure test specimen. The deformation behaviour of the specimen was computed by three-dimensional nonlinear finite element analyses using a recently developed layered 3D-shell element. The distributions of the local mixed mode energy release rates along the initial straight and one measured curved delamination fronts were determined by the virtual crack closure method. The dependency of computed total energy release rate and the individual mode contributions was discussed. By means of 2D-models, using a delamination process element, a curved front was iteratively determined along which the total energy release rate is constant. The obtained front is in good agreement with experimentally observed fronts (figure 27).

From the results of the investigation presented, we conclude the following:

- The hypothesis that the development of the shape of a growing delamination can be predicted using fracture mechanics has been confirmed.
- The results of the investigation indicate that the shape of the delamination contour in angle ply ENF specimens is controlled by $G(s) = G_{II} + G_{III} = const$. This relationship may be regarded as a simple interaction criterion for interlaminar shear failure (mode II/mode III interaction).
- However, a high sensitivity of the energy release rate distribution with respect to the front shape exists, resulting in difficulties when analyzing the energy release rate distributions along experimentally measured delamination contours.
- A strict experimental verification for the interaction criterion requires a smoothed average contour obtained from several experimentally determined fronts, which should then yield a fairly constant G_T along the entire front.
- For multidirectional lay-ups, problems occur when computing mixed mode energy release rates between layers of different orientations (bimaterial interface). This is caused by the

oscillatory nature of the crack tip stress field. For the element sizes and lay-up used in this investigation, an oscillation could not be observed. However, this issue needs to be further investigated using an engineering approach [22, 31, 32].

Acknowledgements

The authors would like to thank Prof. Dr. B.D. Davidson of Syracuse University, New York, for providing the experimental input data, the figure 1, and the C-scan presented in figure 12.

References

- [1] A.G. Miller, D.T. Lovell, and J.C. Seferis. The evolution of an aerospace material: Influence of design, manufacturing and in-service performance. *Composite Structures*, 27:193–206, 1994.
- [2] V.P. McConnel. Getting a fix on repair. *High-Performance Composites*, May/June:19–24, 1994.
- [3] A.C. Garg. Delamination - A damage mode in composite structures. *Eng. Fracture Mech.*, 29(5):557–584, 1988.
- [4] H. Eggers, H.C. Goetting, and H. Bäümel. Synergism between layer cracking and delaminations in MD-laminates of CFRE. In *AGARD Structures and Material Panel*, Patras, Greece, 1992.
- [5] W.G.J. Hart and R.H.W.M. Frijns. Delamination growth in improved carbon composites under constant amplitude fatigue loading. Technical Report NLR TP 89008 U, National Aerospace Laboratory NLR, 1989.
- [6] J.R. Reeder and J.H. Crews Jr. Mixed mode bending method for delamination testing. *AIAA J.*, 28:1270–1276, 1990.
- [7] B.D. Davidson and V. Sundararaman. A Single Leg Bending Test for Interfacial Fracture Toughness Determination. Technical Report No. MAME-94-201, Department of Mechanical, Aerospace and Manufacturing Engineering, Syracuse University, 1994.
- [8] B.D. Davidson and C.S. Altonen. Optimal Geometries and Data Reduction Technique for Unidirectional and Multidirectional End-Notched Flexure Tests. Technical Report No. MAME 93-1001, Department of Mechanical, Aerospace and Manufacturing Engineering, Syracuse University, 1993.
- [9] B.D. Davidson and C.S. Altonen. Effect of Stacking Sequence on Delamination Growth Behaviour and Energy Release Rate in Composite End-Notched Flexure Specimens. Technical Report No. MAME-93-1002, Department of Mechanical, Aerospace and Manufacturing Engineering, Syracuse University, 1993.
- [10] B.D. Davidson, C.S. Altonen, and J.J. Polaha. Effect of Stacking Sequence on Delamination Toughness and Delamination Growth Behaviour in Composite End-Notched Flexure Tests. Technical Report No. MAME-94-402, Department of Mechanical, Aerospace and Manufacturing Engineering, Syracuse University, 1994.
- [11] B.D. Davidson. An analytical investigation of delamination front curvature in double cantilever beam specimens. *J. Composite Mat.*, 24:1124–1137, 1990.
- [12] J.H. Crews Jr., K.N. Shivakumar, and I.S. Raju. Strain energy release rate distribution for double cantilever beam specimens. *AIAA J.*, 29:1686–1691, 1991.

- [13] R. Krüger, M. König, and T. Schneider. Computation of local energy release rates along straight and curved delamination fronts of unidirectionally laminated DCB- and ENF-specimens, AIAA-93-1457-CP. In *The 34th AIAA/ASME/ASCE/AHS/ASC Structures, Structural Dynamics and Materials Conference*, La Jolla, California, pages 1332–1342, 1993.
- [14] R. Krüger. Three Dimensional Finite Element Analysis of Multidirectional Composite DCB, SLB and ENF Specimens. ISD-Report No. 94/2, Institute for Statics and Dynamics of Aerospace Structures, University of Stuttgart, 1994.
- [15] H. Parisch. A continuum-based shell theory for non-linear applications. *Int. J. Num. Meth. Eng.*, 38:1855–1883, 1995.
- [16] S.W. Tsai. *Composite Design*. Think Composites, 4th edition, 1988. ISBN 0-9618090-2-7.
- [17] E.F. Rybicki and M.F. Kanninen. A finite element calculation of stress intensity factors by a modified crack closure integral. *Eng. Fracture Mech.*, 9:931–938, 1977.
- [18] F.G. Buchholz, H. Grebner, K.H. Dreyer, and H. Krome. 2D- and 3D- applications of the improved and generalized modified crack closure integral method. In S.N. Atluri and G. Yagawa, editors, *Computational Mechanics '88*. Springer Verlag, 1988.
- [19] I.S. Raju, K.N. Shivakumar, and J.H. Crews Jr. Three-dimensional elastic analysis of a composite double cantilever beam specimen. *AIAA J.*, 26:1493–1498, 1988.
- [20] K.N. Shivakumar, P.W. Tan, and J.C. Newman Jr. A virtual crack-closure technique for calculating stress intensity factors for cracked three dimensional bodies. *Int. J. Fracture*, 36:R43–R50, 1988.
- [21] I.S. Raju, J.H. Crews, and M.A. Aminpour. Convergence of Strain Energy Release Rate Components for Edge-Delaminated Composite Laminates. *Eng. Fracture Mech.*, 30(3):383–396, 1988.
- [22] C. Hwu and J. Hu. Stress Intensity Factors and Energy Release Rates of Delaminations in Composite Laminates. *Eng. Fracture Mech.*, 42(6):977–988, 1992.
- [23] H. Gao, M. Abbudi, and D.M. Barnett. Interfacial Crack-Tip Field in Anisotropic Elastic Solids. *J. Mech. Phys. Solids*, 40(2):393–416, 1992.
- [24] H. Parisch. A consistent tangent stiffness matrix for three-dimensional non-linear contact analysis. *Int. J. Num. Meth. Eng.*, 28:1803–1812, 1989.
- [25] S. Rinderknecht and B. Kröplin. A finite element model for delamination in composite plates. *Mechanics of Composite Materials and Structures*, 2:19–47, 1995.
- [26] S. Rinderknecht and B. Kröplin. Delamination growth simulation with a moving mesh technique. In B.H.V. Topping and M. Papadrakakis, editors, *Advances in Non-Linear Finite Element Methods*, pages 187–197, 1994. ISBN 0-048749-26-1.

- [27] B.D. Davidson and H. Hu. Effect of Interlayer Modulus on Fracture Mode Ratio for Interleaved Composite Laminates. Technical Report No. MAME-94-204, Department of Mechanical, Aerospace and Manufacturing Engineering, Syracuse University, 1994.
- [28] B.D. Davidson, R. Krüger, and M. König. Three Dimensional Analysis and Resulting Design Recommendations for Unidirectional and Multidirectional End-Notched Flexure Tests. *Journal of Composite Materials*, 29(16):2108–2133, 1995. Also appears as Syracuse University Technical Report No. MAME-94-401, 1994.
- [29] B.D. Davidson, R. Krüger, and M. König. Three Dimensional Analysis of Center Delaminated Unidirectional and Multidirectional Single Leg Bending Specimens. *Composites Science and Technology*, 54(4):385–394, 1995. Also appears as Syracuse University Technical Report No. MAME-94-901, 1994.
- [30] B.D. Davidson, R. Krüger, and M. König. Effect of Stacking Sequence on Energy Release Rate Distributions in Multidirectional DCB and ENF specimens. *Engineering Fracture Mechanics*, 55(4):557–569, 1996. Also appears as Syracuse University Technical Report No. MAME-95-101, 1995.
- [31] C.T. Sun and C.J. Jih. On Strain Energy Release Rates for Interfacial Cracks in Bi-Material Media. *Eng. Fracture Mech.*, 28(1):13–20, 1987.
- [32] C.T. Sun and M.G. Manoharan. Strain Energy Release Rates of an Interfacial Crack Between Two Orthotropic Solids. *J. Composite Materials*, 23:460–478, 1989.

Figures

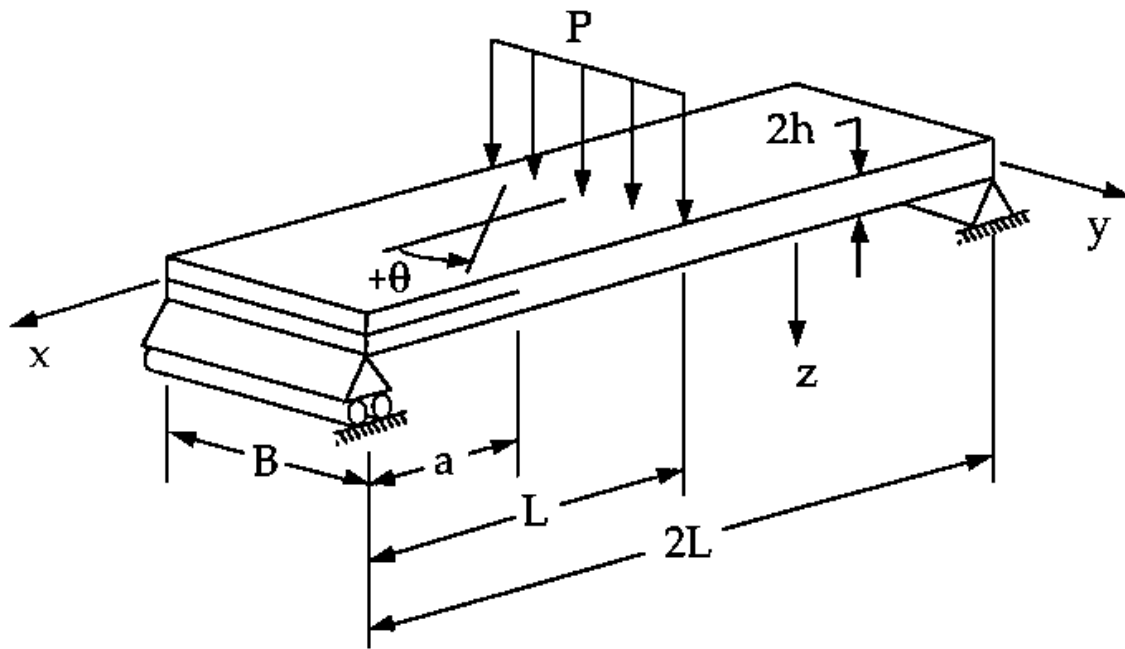


Figure 1: ENF specimen

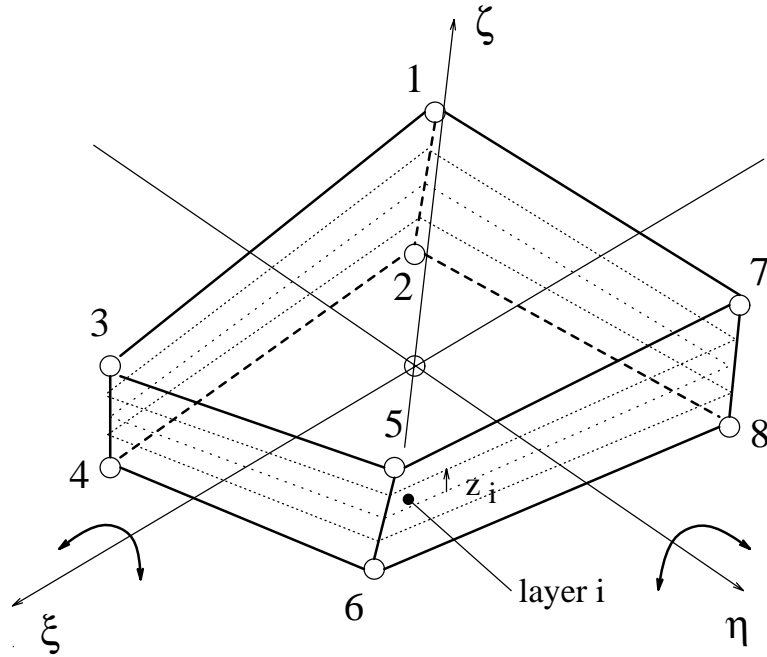


Figure 2: 3D-shell element

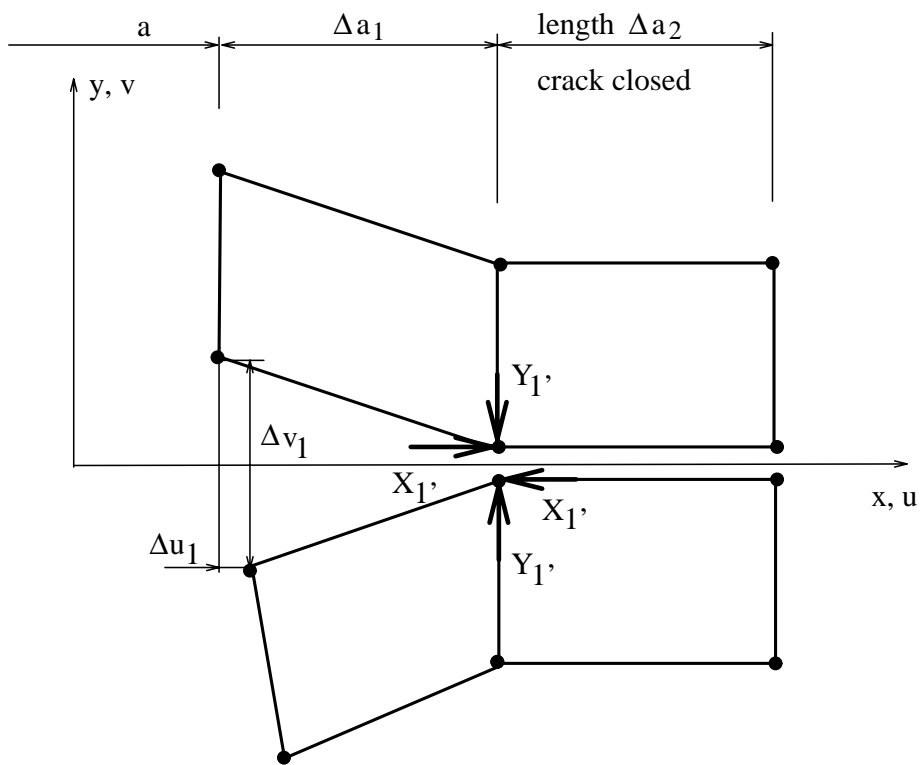


Figure 3: Virtual crack closure method, cut through plane of delamination

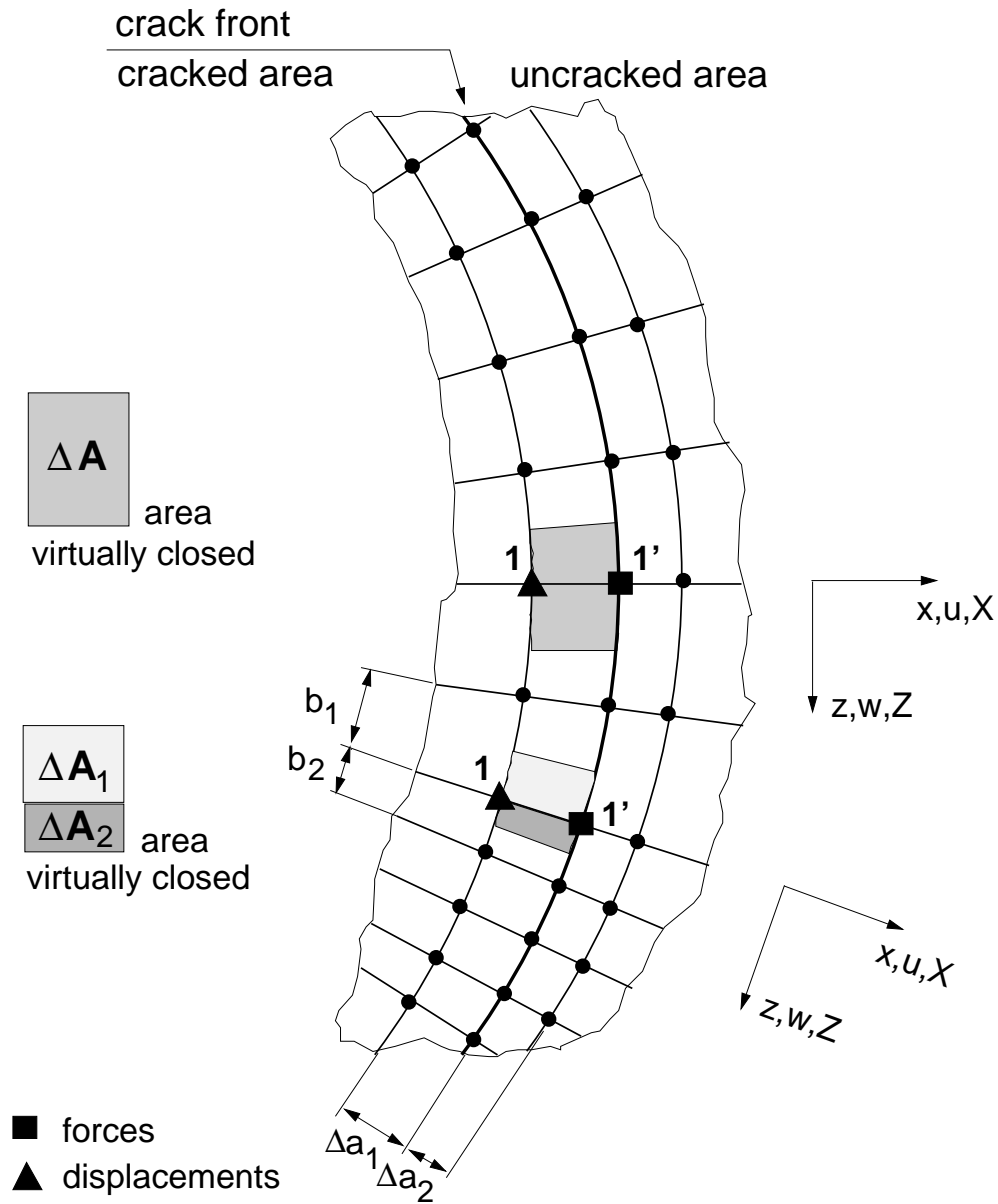


Figure 4: Virtual crack closure method, top view of the plane of delamination

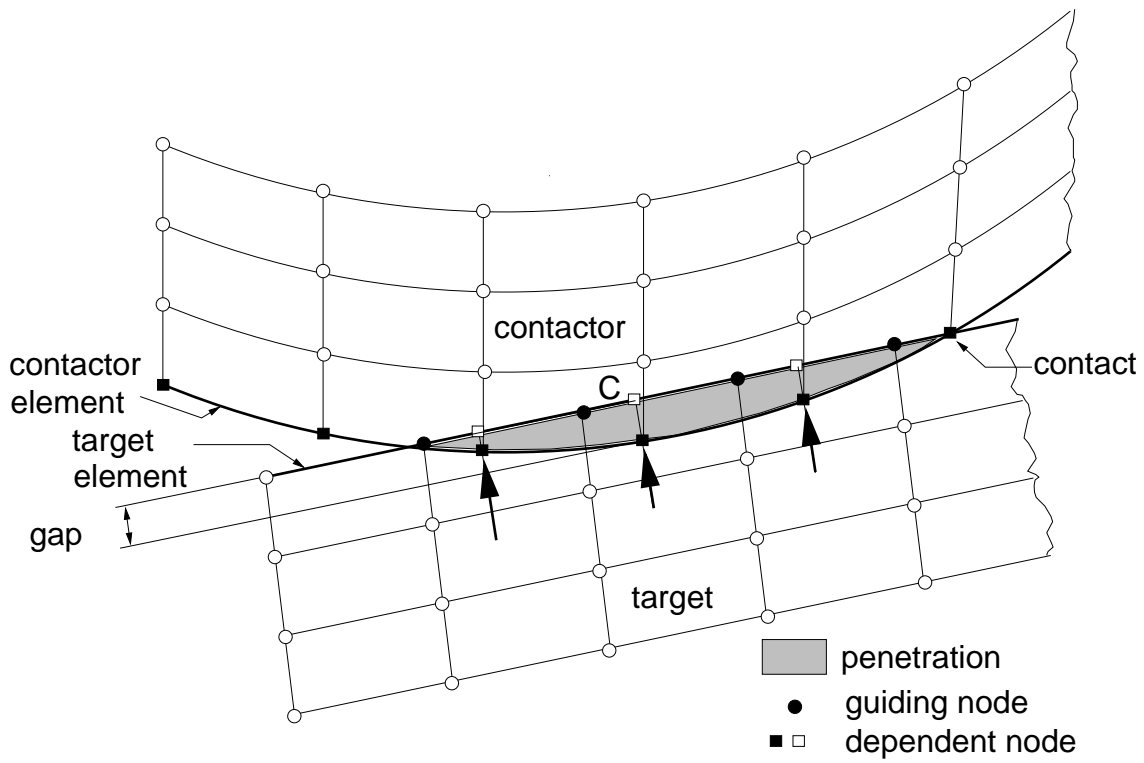


Figure 5: Contact analysis

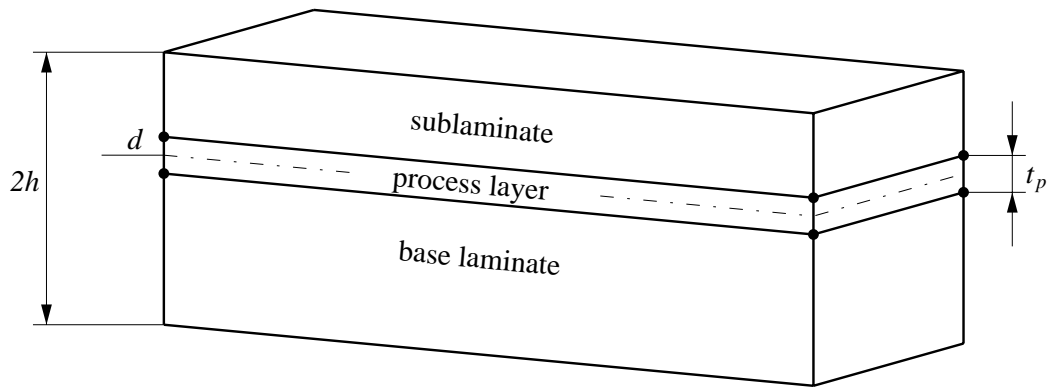


Figure 6: Delamination Process Element

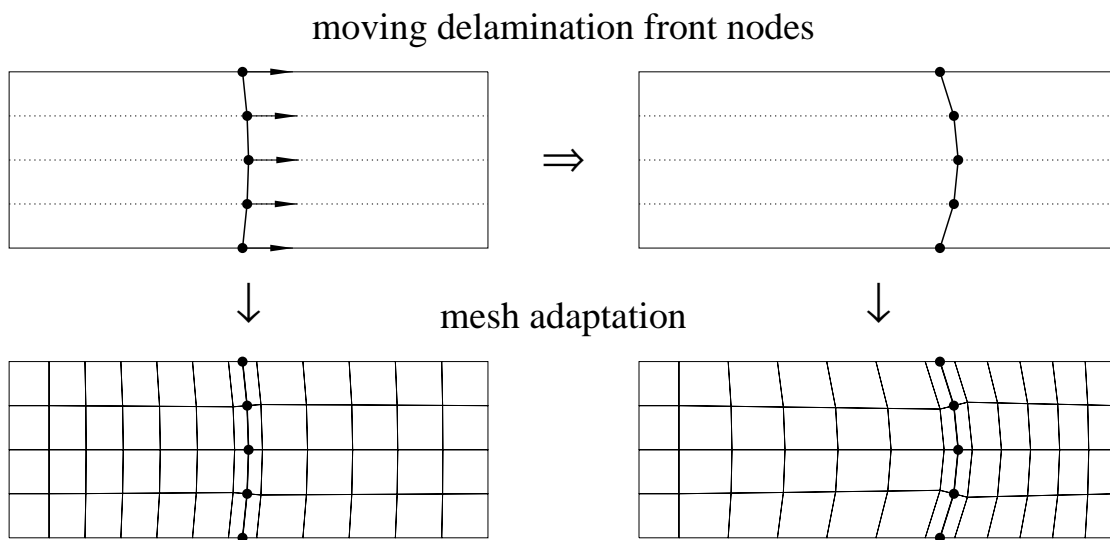


Figure 7: Moving Mesh Technique

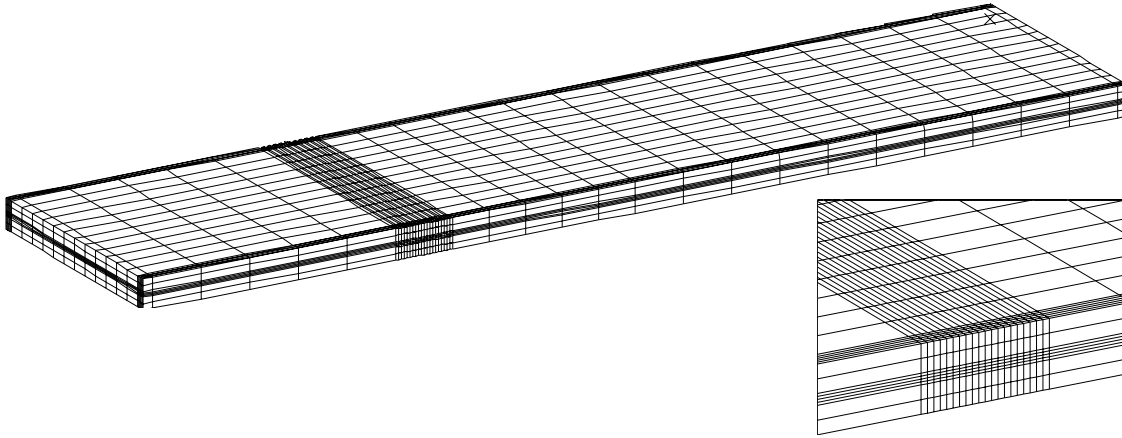


Figure 8: Full width model of ENF specimen

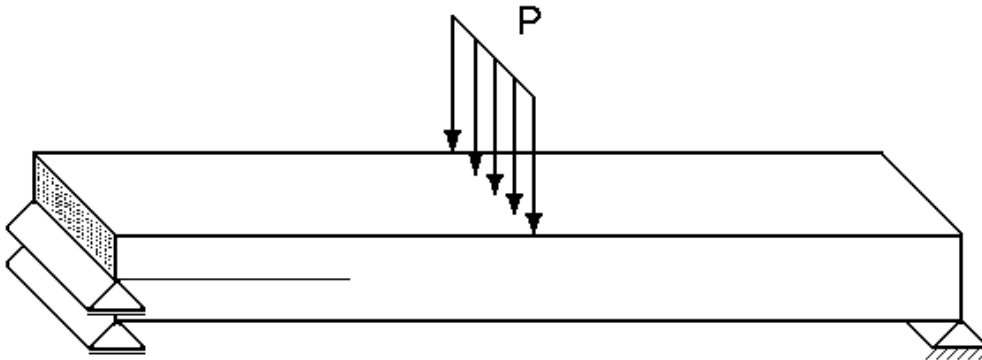


Figure 9: Modified boundary conditions for ENF specimen

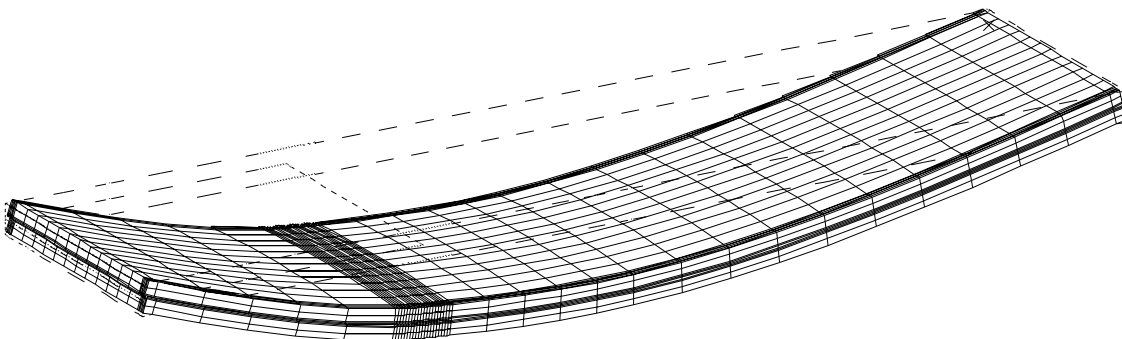


Figure 10: Deformed geometry of ENF specimen (deformation magnified)

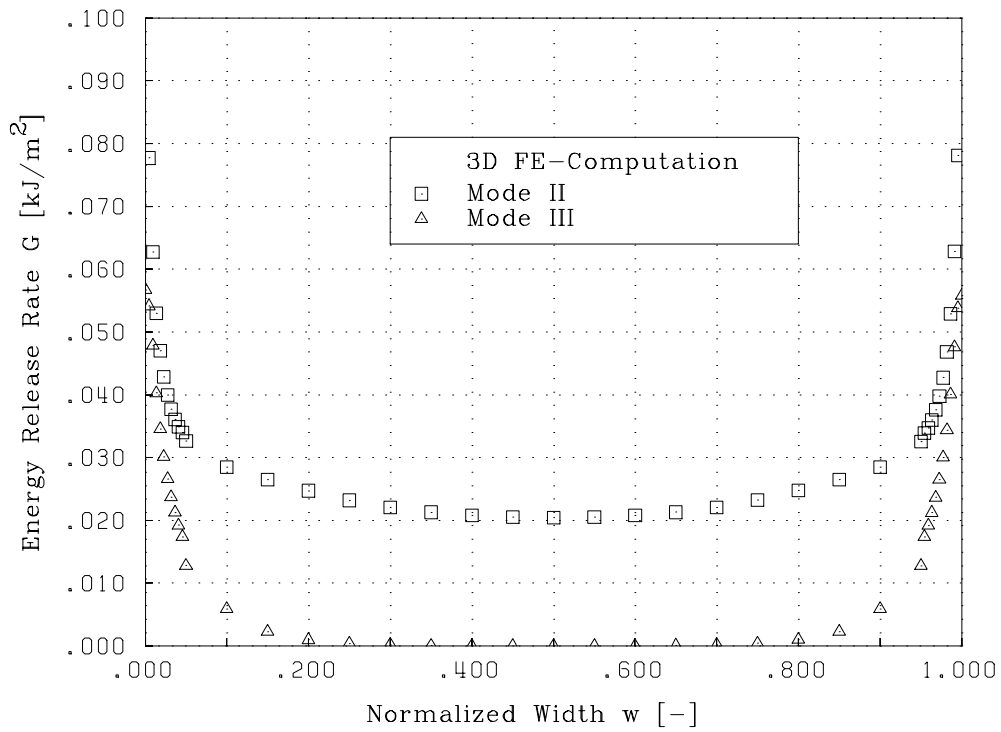


Figure 11: Variation of energy release rates across specimen width for external loading $P = 100$ N

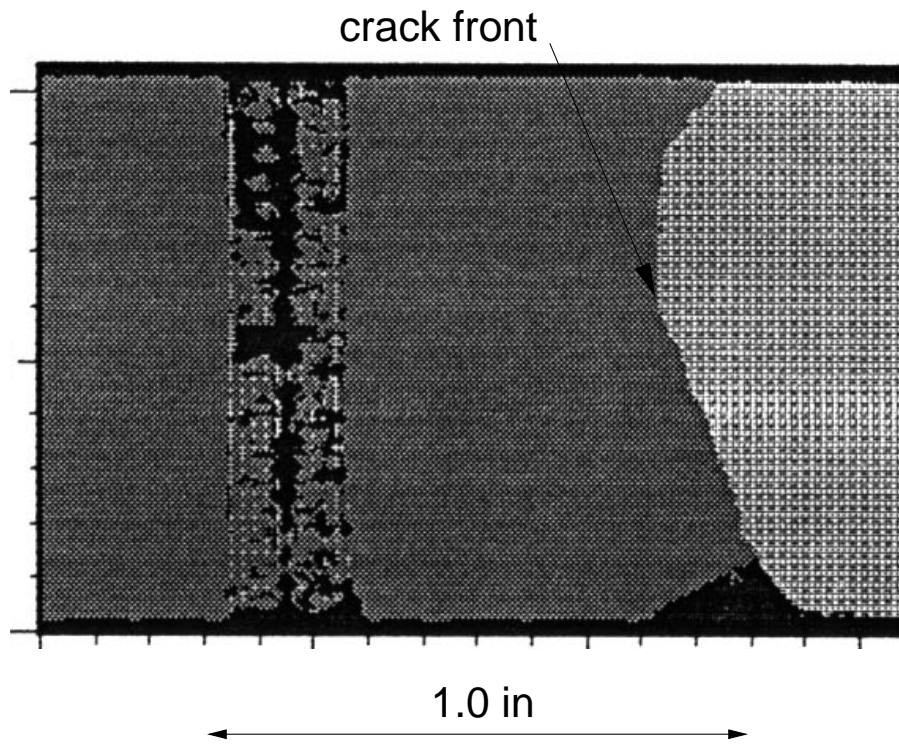


Figure 12: C-scan of ENF specimen with curved front [10]

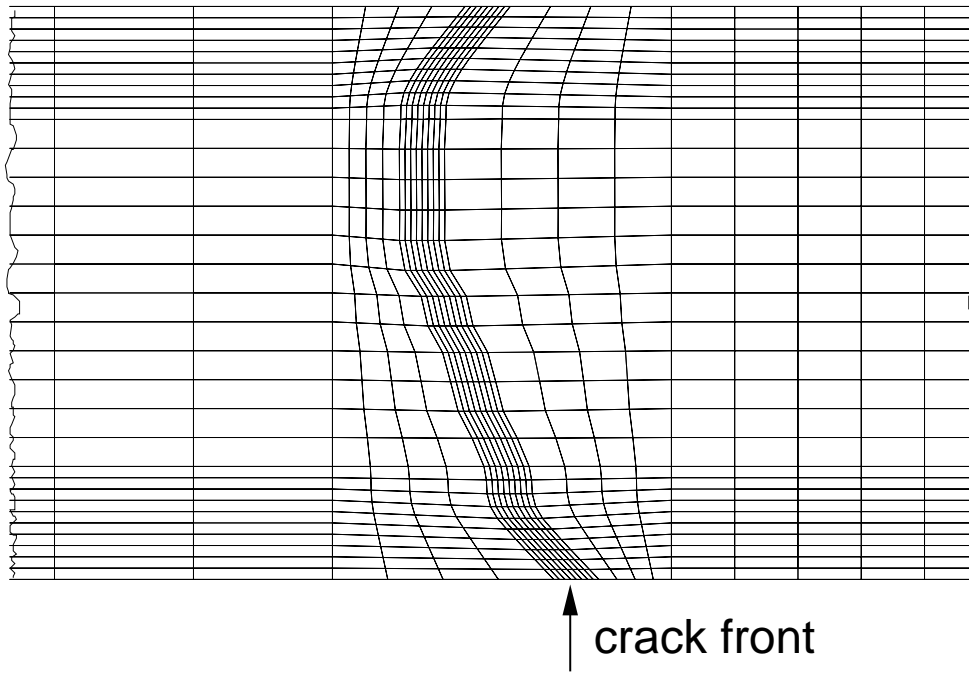


Figure 13: Detail of finite element model around curved front

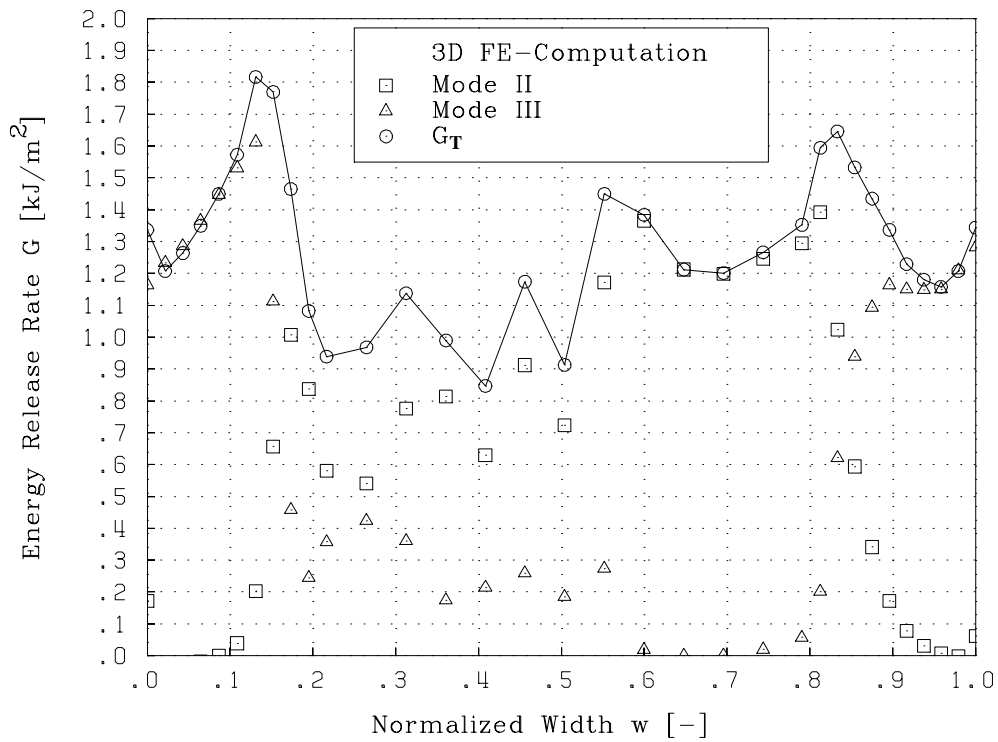


Figure 14: Variation of energy release rates across specimen width for specimen with experimentally determined curved front, external loading $P_c = 601.16$ N

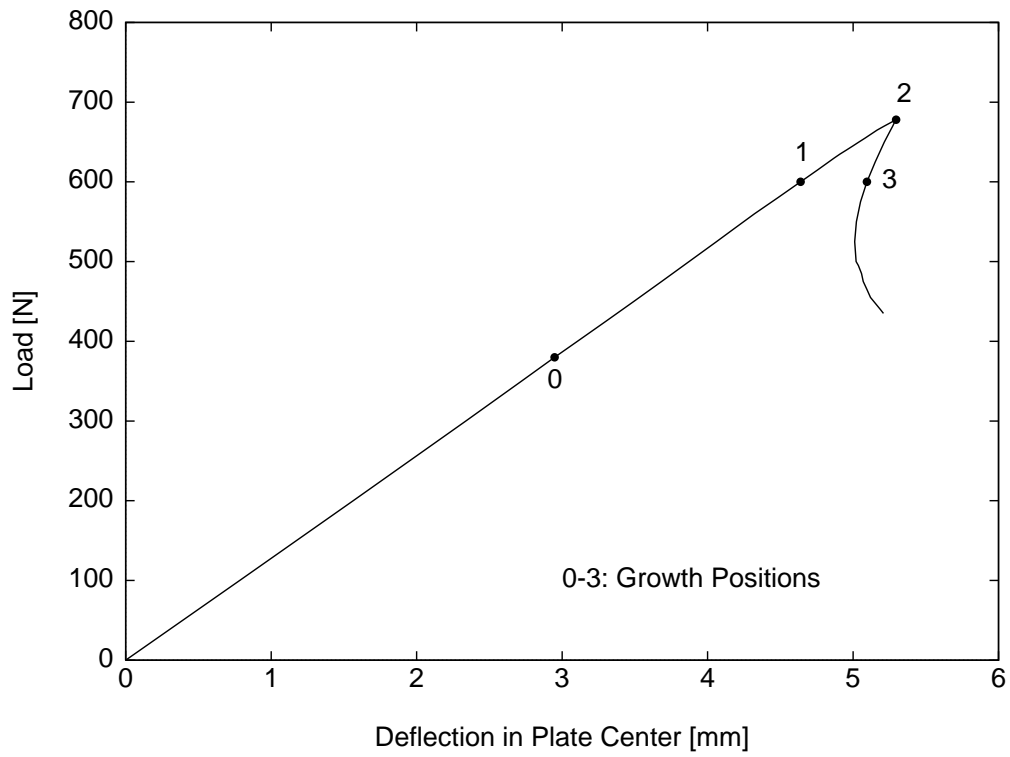


Figure 15: Load-deflection behaviour for ENF specimen (coarse mesh)

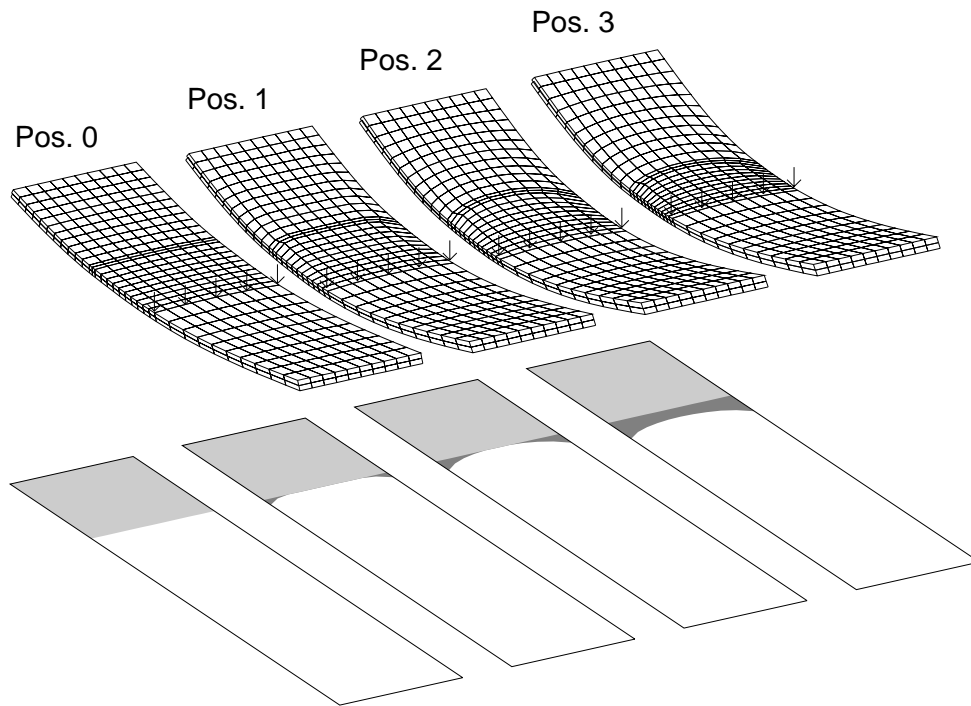


Figure 16: Structural deformation for different growth positions (coarse mesh)

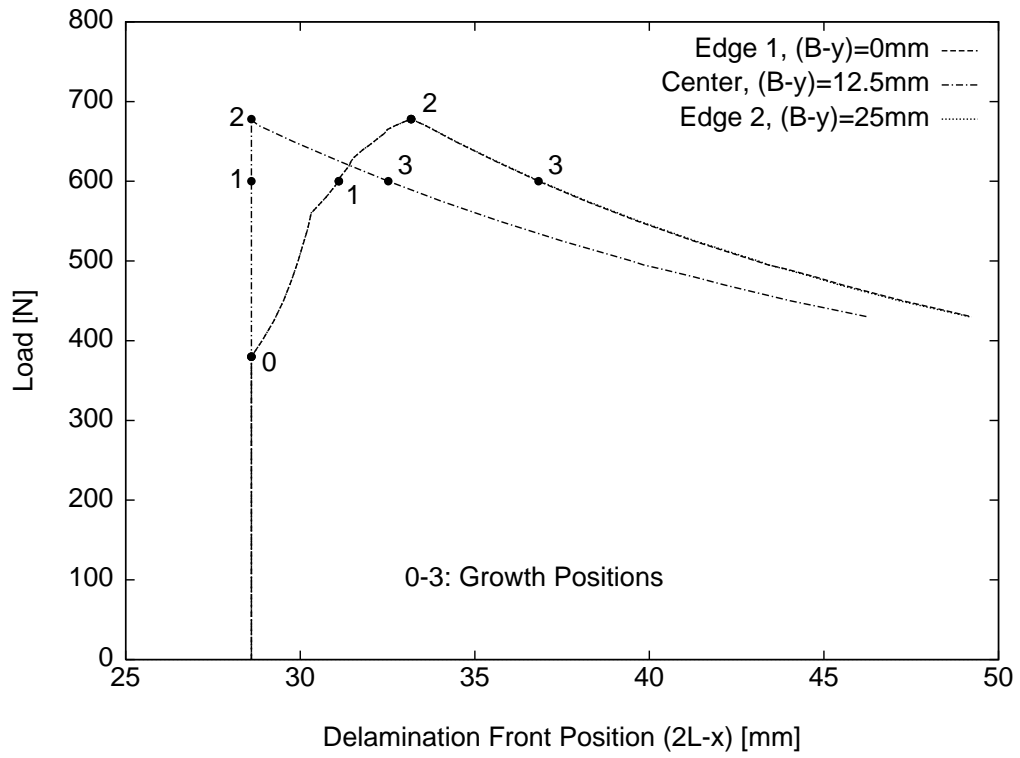
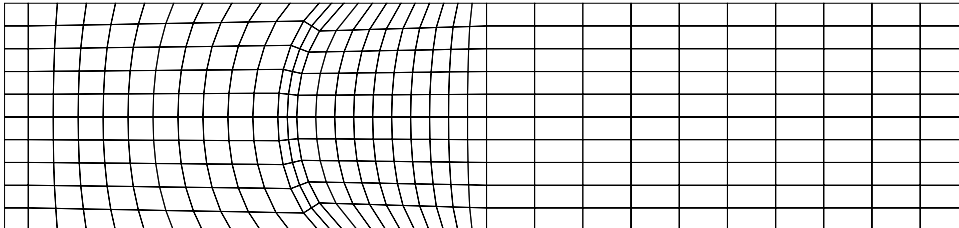


Figure 17: Load-growth behaviour for ENF specimen (coarse mesh)

COARSE MESH WITH GROWTH CONFIGURATION FOR 650 N



FINE MESH WITH GROWTH CONFIGURATION FOR 650 N

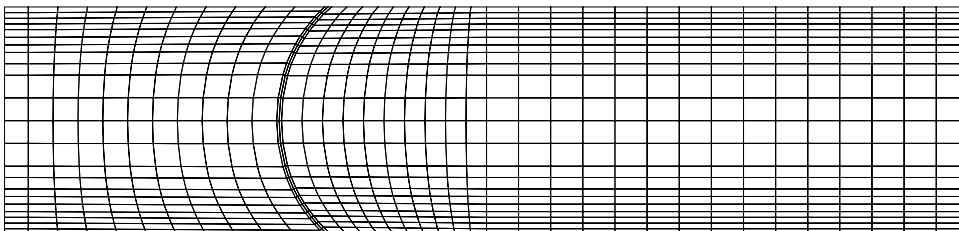


Figure 18: Finite element meshes used for 2D-simulation

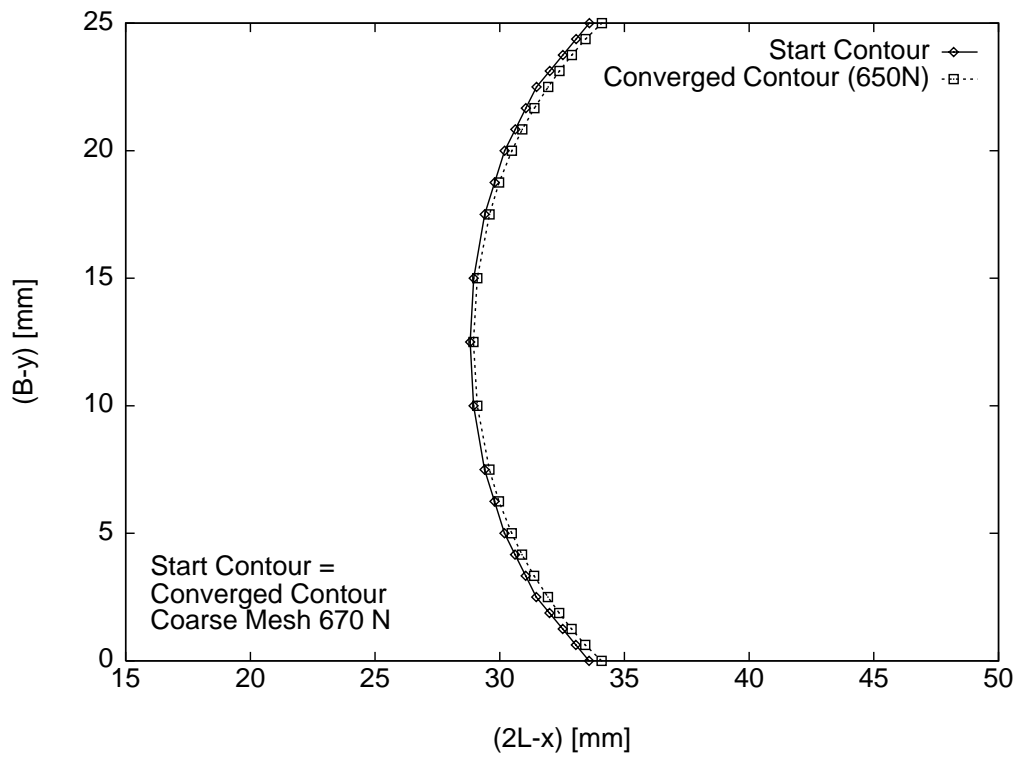


Figure 19: Contour iteration with fine mesh

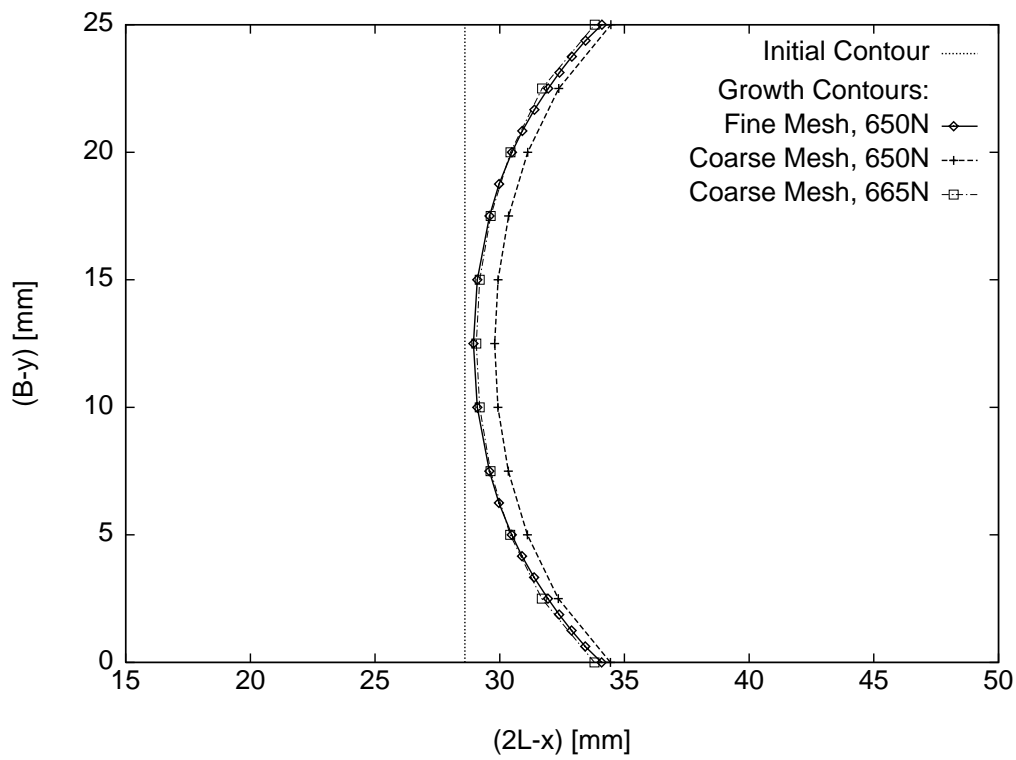


Figure 20: Delamination contours with coarse and fine mesh (unstable growth path)

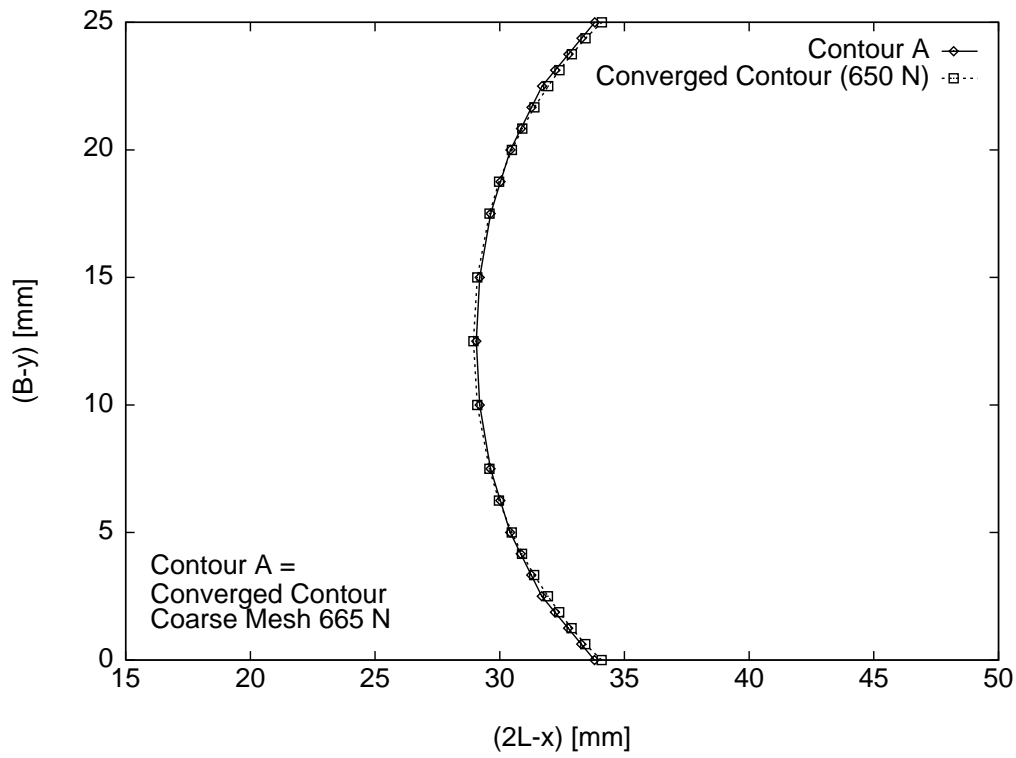


Figure 21: Different front contours for fine mesh

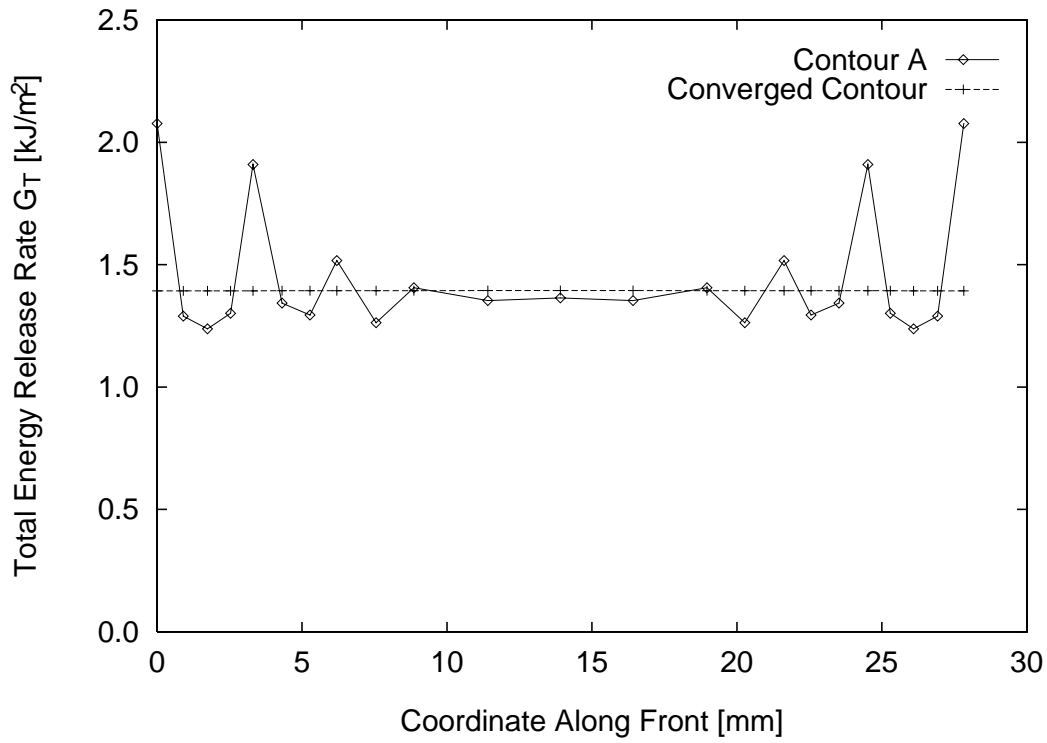


Figure 22: Energy release rates along different front contours (fine mesh, $P = 650$ N)

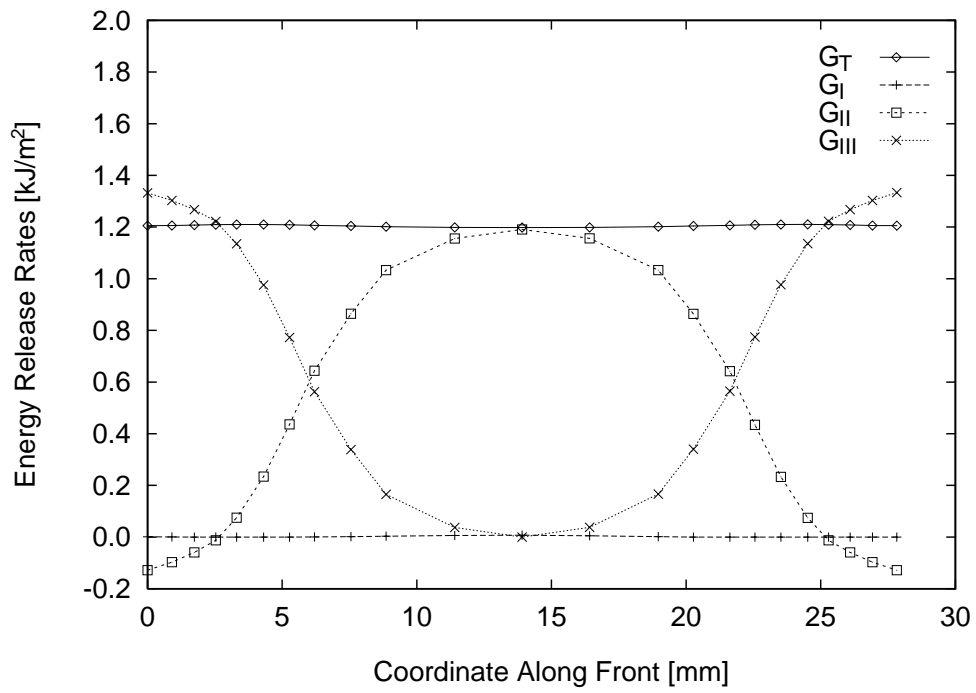


Figure 23: Energy release rates for simulated front (fine mesh, $P_c = 601.16 \text{ N}$)

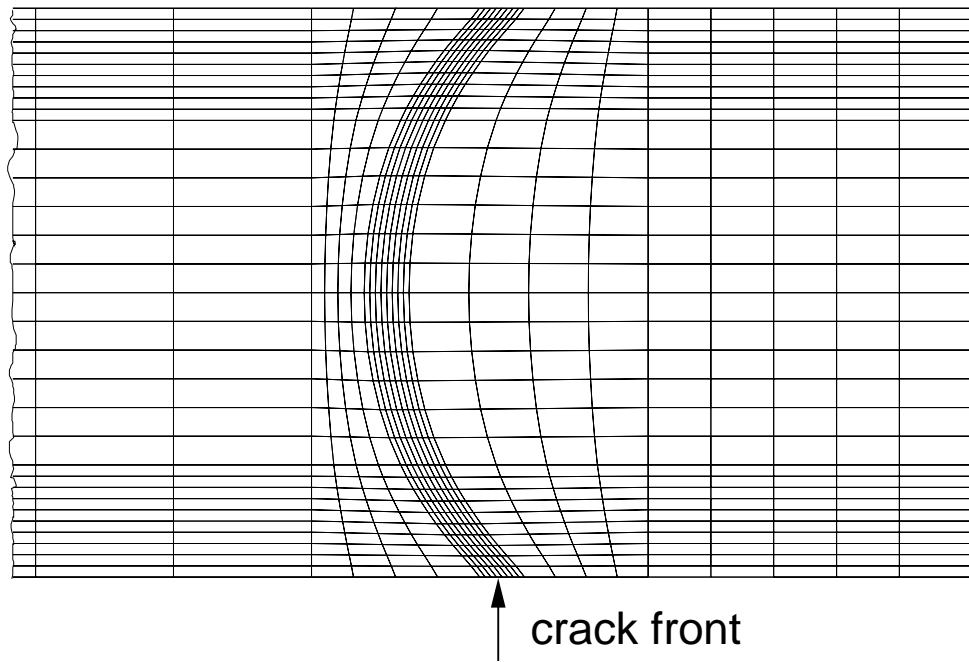


Figure 24: Detail of finite element model around computationally determined curved front

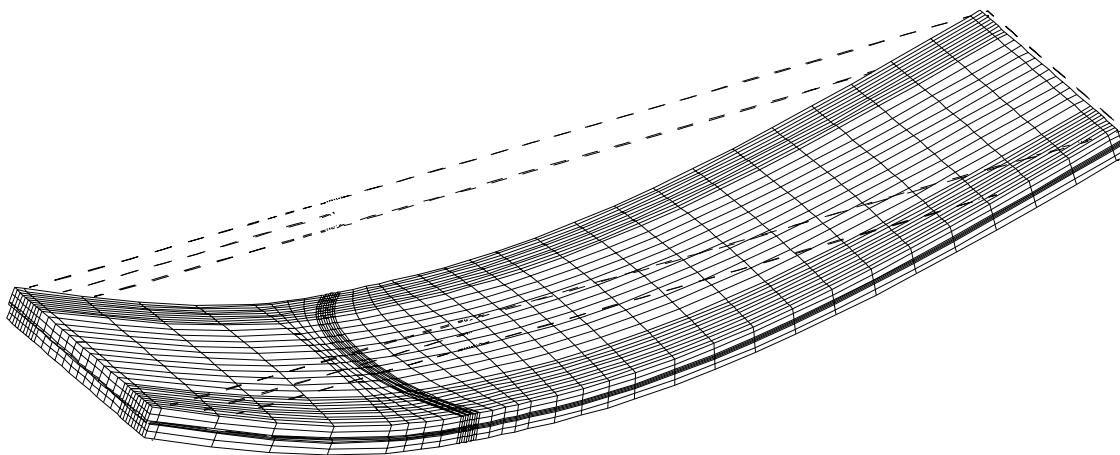


Figure 25: Deformed geometry of ENF specimen with curved front

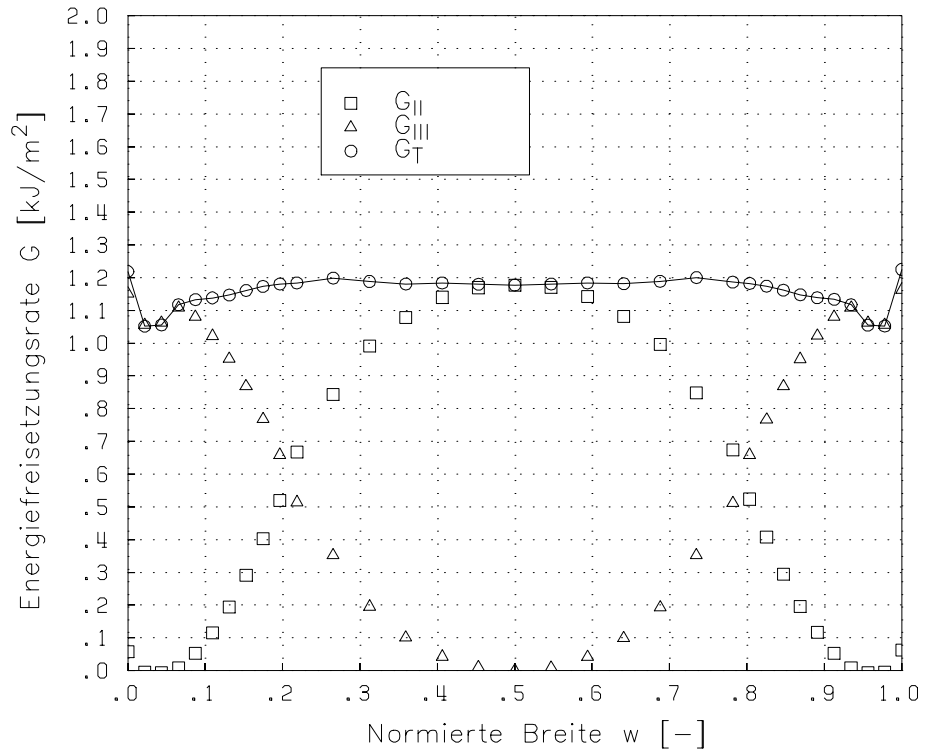


Figure 26: Variation of energy release rates across specimen width for specimen with simulated front ($P_c = 601.16$ N)

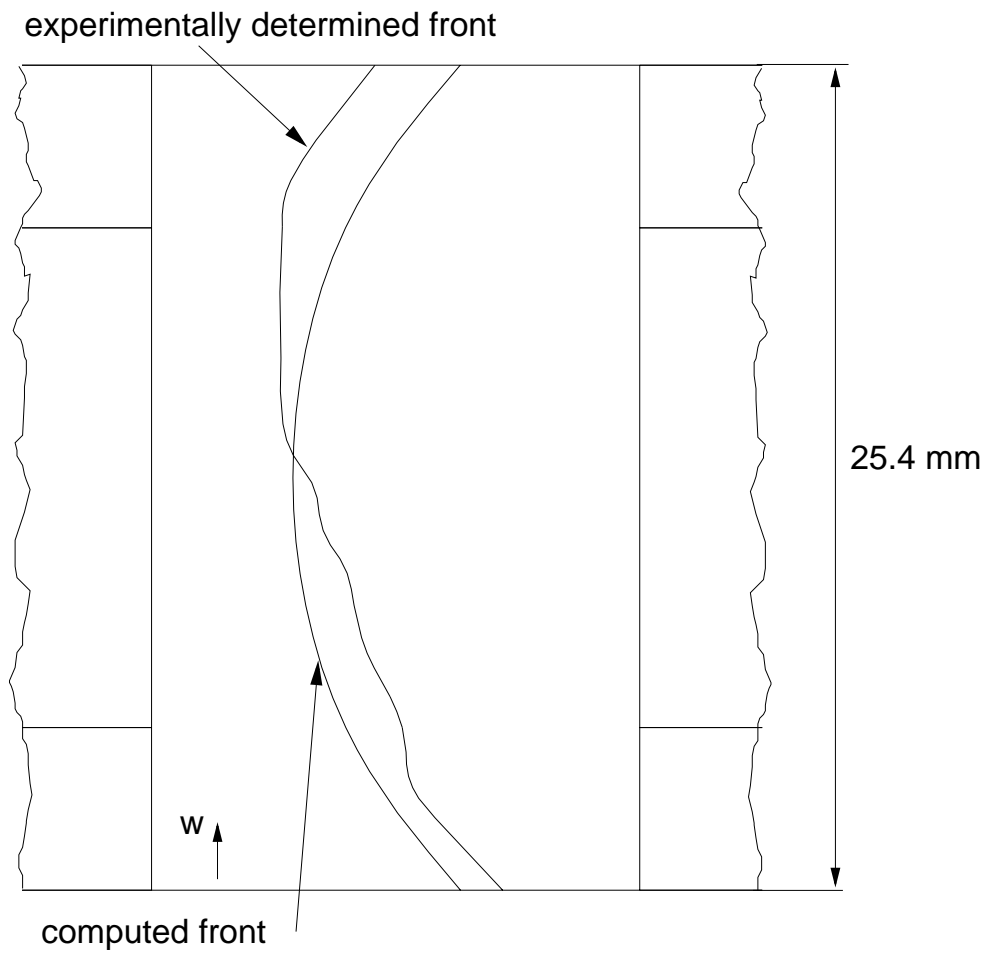


Figure 27: Comparison of experimentally and computationally determined delamination fronts